Delft University of Technology

Estimation of 3D grain size distributions from 2D sections in real and simulated microstructures

Jagt, Thomas van der; Vittorietti, Martina; Sedighiani, Karo; Bos, Cornelis; Jongbloed, Geurt

Important note
To cite this publication, please use the final published version (if applicable).
Please check the document version above.

Contents lists available at ScienceDirect

Computational Materials Science

journal homepage: www.elsevier.com/locate/commatsci

Full length article

Estimation of 3D grain size distributions from 2D sections in real and simulated microstructures

Thomas van der Jagt [a],*, Martina Vittorietti [a], Karo Sedighiani [b], Cornelis Bos [b,c], Geurt Jongbloed [a]

[a] *Department of Applied Mathematics, Delft University of Technology, Mekelweg 4, Delft, 2628 CD, The Netherlands*
[b] *Tata Steel Research & Development, PO Box 10000, IJmuiden, 1970 CA, The Netherlands*
[c] *Department of Materials Science and Engineering, Delft University of Technology, Mekelweg 2, Delft, 2628 CD, The Netherlands*

ARTICLE INFO

ABSTRACT

Obtaining information about the 3D grain size distribution of metallic microstructures is crucial for understanding the mechanical behavior of metals. This paper addresses the problem of estimating the 3D grain size distribution from 2D cross sections. This is a well-known stereological problem and different estimators have been proposed in the literature. We propose a statistical estimation procedure that provides consistent estimates without relying on arbitrary binning choices. When applying this procedure to space filling structures, we investigate the impact of the choice of grain shape and propose a heuristic to choose the best grain shape. To validate our approach, we employ simulations using Laguerre–Voronoi diagrams and apply our methodology to a sample of Interstitial-Free steel, obtained via EBSD.

1. Introduction

Polycrystalline materials, composed of multiple grains with distinct crystallographic orientations, exhibit intricate microstructures that significantly influence their mechanical properties [1]. Different types of microstructure-based simulations depend on proper estimation and characterization of the microstructure [2]. For example, a thorough physical understanding of the underlying mechanisms behind phenomena such as local stress fields [3,4], fracture and damage initiation [5–7], shear banding [8–10], and recrystallization nucleation [11–13] depends on the initial microstructure. In addition to the microscale mechanical response, the macroscopic mechanical response, such as the stress–strain curve and yield surface, also depends on the microstructure [14–19]. Therefore, accurate characterization of the microstructure of polycrystalline materials is essential and has become a crucial part of materials science research. One of the critical microstructural features is the grain size distribution, which can affect many mechanical responses [14,20]. For example, at a macro scale, it can affect the stress–strain curve. At a smaller scale, it can influence the stress and strain localization [9,21], impacting for instance damage evolution. However, direct 3D measurement of the grain size distribution is costly and time-consuming [22]. Instead, more common two-dimensional (2D) characterization techniques, such as light microscopy, Scanning Electron Microscopy (SEM), and Electron Backscatter Diffraction (EBSD), are employed. These 2D techniques provide only

surface information, leaving part of the critical information, like the 3D grain size distribution, unknown. This paper aims to use 2D information obtained from section areas to estimate the 3D grain size distribution, offering a more efficient and accessible approach to microstructure characterization. Estimating the 3D grain size distribution from 2D observations is a well-known stereological problem, originally addressed by [23], in the so called Wicksell corpuscle problem. In the Wicksell model, grains are represented by spheres of varying size, randomly positioned in 3D space. Intersecting this system of spheres with a plane results in a sample of observed circle radii, the distribution of which is uniquely related to the distribution of the 3D sphere radii.

However, when considering real microstructures, the assumption of (approximately) spherical grains is often unrealistic. A more realistic approach is to generalize the Wicksell model by replacing spheres with another convex shape, such as a polyhedron. Such a polyhedron then represents the typical grain shape. Instances of this polyhedron are randomly scaled, -oriented and -positioned in 3D space. Intersecting this system with a plane yields observed section profiles, the areas of which can be used to estimate the grain size distribution.

Various estimation procedures have been developed for these stereological problems. For spherical grains (Wicksell's problem), the Saltykov method [24] is widely used, estimating the underlying radius distribution as a discrete histogram, requiring bin size choices.

---

* Corresponding author.
 E-mail address: T.F.W.vanderJagt@tudelft.nl (T. van der Jagt).

Numerous variations of the Saltykov method exist, often differing in binning strategies, inversion procedures, or the choice of parametric distributions [25–27]. Other methods extend these principles to non-spherical grains, such as cubes or other specific polyhedra [28–31]. For a more elaborate overview of estimators in the Wicksell problem we refer to [32].

In [33] a new estimation procedure is proposed, offering a discrete distribution estimate for grain size via non-parametric maximum likelihood estimation. This method, when the shape of the 3D objects is known and fixed, is consistent, meaning that as the sample size increases, the estimate converges to the true distribution. Unlike the Saltykov method, which typically uses a fixed number of bins, this new method implicitly optimizes the number and size of bins through likelihood maximization, eliminating the need for manual binning.

The estimation procedure used in this paper, was developed (and theoretically studied) in [33] from the perspective of randomly placed, scaled and oriented particles in a 3D medium. In practice, this type of procedures is commonly applied to space-filling structures, often seen in metal microstructures. As this procedure works for arbitrary convex shapes, it enables to investigate which of these shapes actually works best in specific situations with space-filling structures.

In this paper we apply this estimation method to various simulated- and real microstructures. We explore a range of grain shapes to assess how the chosen shape relates to the estimation accuracy of the actual grain size distributions. In the simulation setting, we consider Voronoi and the more general Laguerre–Voronoi diagrams as models for metal microstructures. These diagrams provide realistic approximations of grain shapes and distributions found in metals [34], making them ideal for studying the accuracy of 3D grain size distribution estimations derived from 2D cross-sectional images. In fact, though several theoretical properties of these models are known in the literature [35–37], there are no explicit relations or estimators of the 3D volume distributions from the 2D sections. Hence, applying the estimation procedure proposed in this paper in a simulation setting can provide insights into the behavior of the estimator for the underlying model.

The contributions in this paper are the following: (i) we estimate the 3D grain size distribution using a novel statistical estimation procedure; (ii) we investigate the influence of assumed grain shapes on the estimation of grain size distributions; (iii) we conduct extensive simulations using random 3D (Laguerre)-Voronoi microstructures and single planar sections to estimate the underlying grain size distribution; and (iv) we show that for the considered microstructures, a few grain shape choices yield accurate estimates, providing a practical procedure for selecting appropriate shapes for steel samples.

The outline of the paper is as follows: in Section 2 we describe the estimation procedure used for obtaining the 3D grain size distributions. Furthermore, we illustrate the methods used for the simulation of microstructures, as well as how cross sections are taken of these simulated microstructures. In Section 3, the simulation results for 100 Laguerre Voronoi diagrams are presented. Estimates based on different shapes for the grains are compared and in Section 4 a heuristic of the choice of the best shape is discussed. In Section 5 the new estimation procedure is applied to real data. In this special case, the results of the volume distribution estimation based on 2D real data can be compared with the real 3D volume distribution obtained based on the 3D EBSD data. Final considerations and conclusions are discussed in Sections 6 and 7.

2. Methods

In this section, we present the estimation procedure used to determine the grain size distributions (Section 2.1). Additionally, we describe the simulation procedure of the microstructures and the process of obtaining cross sections from these simulations (Section 2.2).

2.1. Estimation of grain size distributions

We briefly summarize the estimation procedure, introduced in [33]. Assume we have a sample of observed section areas: $a_1, a_2, \ldots, a_n$, with n being the sample size. This is assumed to be the sorted sample, meaning that: $a_1 < a_2 < \cdots < a_n$. We assume a particular 3D grain shape $K \subset \mathbb{R}^3$, representing the typical grain in the microstructure at hand. Consider taking a random section of the chosen shape K, which is scaled such that it has volume 1. The probability density function associated with the square-root of the area of such a random section is denoted by g_K^S. In principle g_K^S becomes known once the shape is chosen; in practice we use simulations to obtain a very close approximation of this function. The estimation procedure can be described by two steps. First we estimate a biased size distribution, both for mathematical as well as computational convenience. This can be interpreted as the distribution of the size of the typical grain which appears in the section plane. It is well known that larger grains are more likely to be hit by the section plane, meaning that larger grains are over represented in the plane section. Therefore, the actual grain size distribution is different, and it is estimated in a second step via a de-biasing procedure. Denote by H the size distribution function. The two steps of the procedure are:

- **Step 1**: Estimation of the length-biased size distribution function H^b associated with H

$$H^b(\lambda) = \frac{\int_0^\lambda x \, dH(x)}{\int_0^\infty x \, dH(x)}. \tag{1}$$

Set $s_i = \sqrt{a_i}$ for $i \in \{1, \ldots, n\}$ and denote by $\mathcal{F}_n^+$ the set of all piecewise constant CDFs (Cumulative Distribution Functions) on $[0, \infty)$, having jumps at the observed s_i's. The maximum likelihood estimator $\hat{H}_n^b$ for H^b is then defined as a maximizer of the log-likelihood:

$$\hat{H}_n^b = \arg\max_{H^b \in \mathcal{F}_n^+} \frac{1}{n} \sum_{i=1}^n \log\left(\sum_{j=1}^n g_K^S\left(\frac{s_i}{s_j}\right) \frac{1}{s_j} (H^b(s_j) - H^b(s_{j-1})) \right)$$

Since the log-likelihood is a concave function, this optimization problem is computationally tractable, and has only a global maximizer. After solving this optimization problem we obtain the vector $(\hat{H}_n^b(s_1), \hat{H}_n^b(s_2), \ldots, \hat{H}_n^b(s_n))$, representing the values of the estimate evaluated at $s_1, s_2, \ldots, s_n$.

- **Step 2**: De-biasing the estimate of the length-biased size distribution. The de-biased distribution function H can be expressed in H^b by inverting (1). Using this inverse leads to instabilities due to the occurrence of very small s_i-values. Therefore we use the following estimator of the size distribution function H, denoted by $\hat{H}_n$:

$$\hat{H}_n(\lambda) = \begin{cases} \frac{\int_{t_n}^\lambda \frac{1}{x} d\hat{H}_n^b(x)}{\int_{t_n}^\infty \frac{1}{x} d\hat{H}_n^b(x)} & \text{if } \lambda \geq t_n \\ 0 & \text{if } 0 \leq \lambda < t_n \end{cases}$$

Here, t_n is a tuning parameter which leads to a more stable inverse (direct inversion of (1) would lead to the choice $t_n \equiv 0$). For $t > 0$ the truncated version of $\hat{H}_n^b$ is given by:

$$\hat{H}_n^b(\lambda; t) = \begin{cases} \frac{\hat{H}_n^b(\lambda) - \hat{H}_n^b(t)}{1 - \hat{H}_n^b(t)} & \text{if } \lambda \geq t \\ 0 & \text{otherwise} \end{cases}$$

In order to choose the tuning parameter t_n, write G_K^S for the CDF corresponding to g_K^S and define for $s \geq 0$

$$\hat{F}_n^S(s; t) := \int_0^\infty G_K^S\left(\frac{s}{\lambda}\right) d\hat{H}_n^b(\lambda; t).$$

This may be interpreted as the distribution of the square-root areas if $\hat{H}_n^b(\cdot; t)$ were the true underlying biased distribution. We
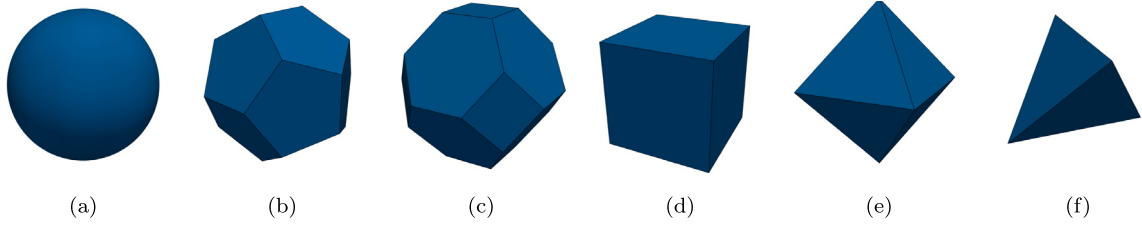
Fig. 1. (a): Sphere. (b): Dodecahedron. (c): Kelvin cell/ Tetrakaidecahedron. (d) Cube. (e): Octahedron. (f): Tetrahedron.
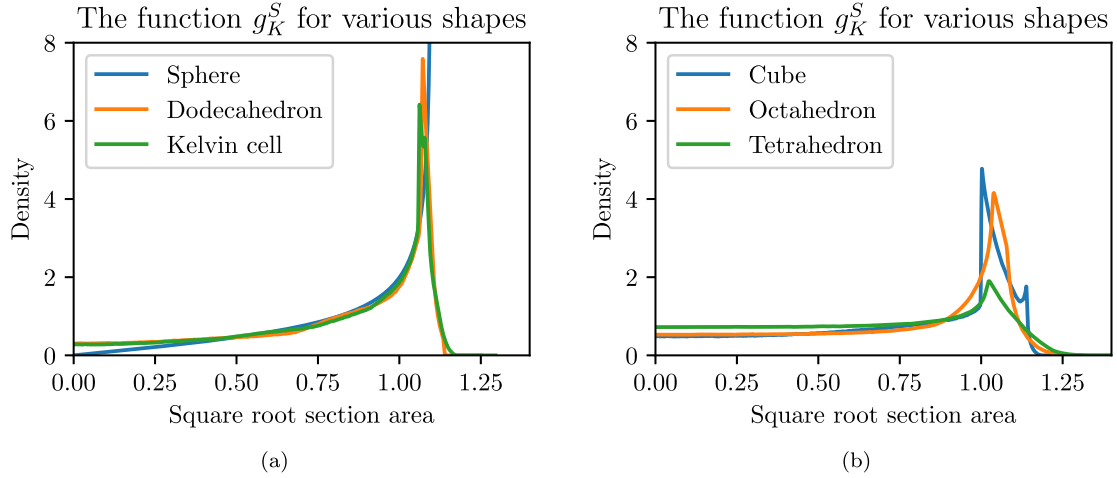

Fig. 2. The function g_K^S for the shapes shown in Fig. 1.

also define:

$$\bar{F}_n^S(s) := \frac{1}{n} \sum_{i=1}^{n} \mathbb{1}\{s_i \le s\},$$

the empirical distribution of the observed square-root areas $s_1, s_2, \ldots, s_n$. Then, we use the following choice for the tuning parameter t_n:

$$\hat{t}_n := \underset{t \in \{s_1, \ldots, s_n\}}{\arg\min} \int_0^\infty |\hat{F}_n^S(s; t) - \bar{F}_n^S(s)| \, \mathrm{d}s. \tag{2}$$

Hence, $\hat{t}_n$ minimizes the L_1-distance between the CDF of the square root section areas, induced by the estimated (biased) size distribution, and the empirical CDF of the actually observed square root section areas. In practice the integral in (2) can be computed via numerical integration. One should then keep in mind that $\bar{F}_n$ is a piecewise constant function while $\hat{F}_n^S$ is not. This procedure yields an estimate of the size distribution function H. A grain with size $\lambda > 0$ is up to a translation and rotation equal to λK. By λK we mean that K is scaled with a factor λ. As such, a grain with size λ has volume: $\text{Volume}(\lambda K) = \lambda^3 \text{Volume}(K) = \lambda^3$. As a result the size distribution is related to the volume distribution function F_V via: $F_V(x) = H(x^{\frac{1}{3}})$. Hence, we estimate F_V as: $\hat{F}_V(x) = \hat{H}_n(x^{\frac{1}{3}})$. Additionally, the so-called biased volume distribution is given by $F_V^b(x) = H^b(x^{\frac{1}{3}})$ and may be estimated via $\hat{F}_V^b(x) = \hat{H}_n^b(x^{\frac{1}{3}})$. For simulations, we consider the shapes shown in Fig. 1. For each shape K, we need the function g_K^S to carry out the estimation procedure. For all the considered shapes the function g_K^S is shown in Fig. 2.

2.2. Simulation of random microstructures

We first describe the model chosen for our simulations. For studying the behavior of the estimator proposed in the previous section we run simulations using Voronoi diagrams as mathematical model for microstructures. Voronoi diagrams and its generalizations are often

referred as the state of the art for modeling microstructures [34]. Given some convex domain Ω in 3D space, a Voronoi diagram divides Ω into so-called cells, which are convex polyhedra. Given distinct points $x_1, \ldots, x_N \in \Omega$ and denoting by $\| \cdot \|$ the Euclidean norm, the Voronoi diagram generated by these points has cells $C_1, \ldots, C_N$ with:

$$C_i = \{x \in \mathbb{R}^3 : \|x - x_i\| \le \|x - x_j\|, \text{ for all } j \in \{1, \ldots, N\}\}.$$

In this paper, we consider the Poisson–Voronoi diagram, meaning that the x_i's are a realization of a homogeneous Poisson process Φ on Ω. While Voronoi diagrams are attractive models for materials microstructures, the additional flexibility of its generalization, the Laguerre Voronoi diagrams, also referred as Laguerre diagrams, allows to more accurately model real microstructures. In [38] it was observed that geometric characteristics of Laguerre diagrams were closer to geometric characteristics of real polycrystalline microstructures in comparison to Voronoi diagrams. In [36,39] Laguerre diagrams were demonstrated to accurately model a foam microstructure. Moreover, [36] showed that Laguerre diagrams provided a better representation of foams compared to various types of Voronoi diagrams. The results in [40] indicate that Laguerre diagrams provide a superior representation for sintered alumina than Voronoi diagrams. Additionally, [41] demonstrated that Laguerre diagrams can accurately model two-phase composites.

Given some convex domain Ω in 3D space, a Laguerre diagram also divides Ω into cells, which are convex polyhedra. Given distinct points $x_1, \ldots, x_N \in \Omega$ and weights: $w_1, \ldots, w_N \in \mathbb{R}$. A Laguerre diagram generated by these weighted points has cells $L_1, \ldots, L_N$ with:

$$L_i = \{x \in \mathbb{R}^3 : \|x - x_i\|^2 - w_i \le \|x - x_j\|^2 - w_j, \text{ for all } j \in \{1, \ldots, N\}\}.$$

The Voronoi diagram is obtained if all weights are equal: $w_1 = w_2 = \cdots = w_N$. Hence, in order to describe how Laguerre diagrams are generated we need to specify how we choose the weights. A Laguerre diagram with periodic boundary conditions may be obtained by replacing the Euclidean distance $\| \cdot \|$ with a periodic distance.
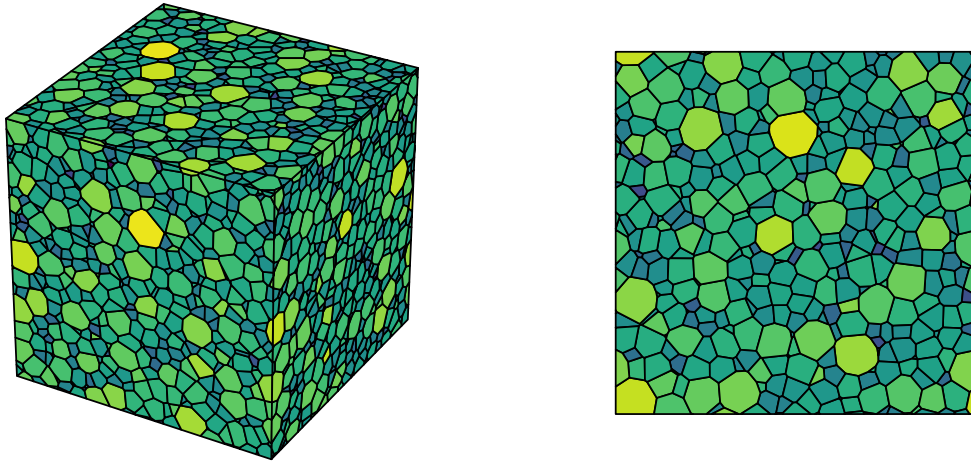
Fig. 3. Example of a 3D Laguerre–Voronoi diagram with periodic boundary conditions, and a 2D planar section. Cells are colored according to their 3D volume.
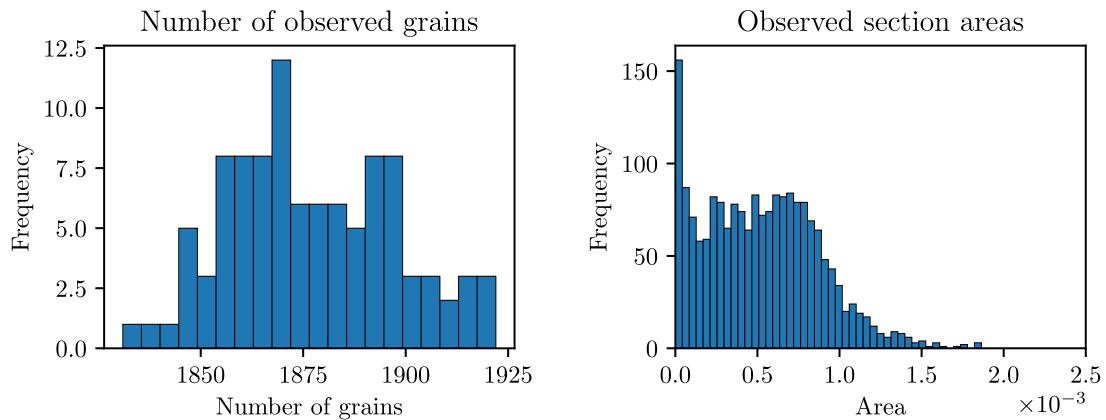

Fig. 4. Left: Histogram of the number of observed grains for each of the 100 simulations. Right: Histogram of the observed section areas from one simulation.

We now describe the simulation setting. First, we define the domain as the unit cube $\Omega = [0,1] \times [0,1] \times [0,1]$. We fix a number of grains N, and generate a Poisson process conditioned on having N grains, that is equivalent to sample N uniformly distributed points: $x_1, \dots, x_N$ in Ω. We choose a volume distribution function F_V and sample $v_1, \dots, v_N \overset{iid}{\sim} F_V$. Then, we set:

$$r_i = \frac{v_i}{\sum_{i=1}^{N} v_i},$$

such that the r_i's represent the volume fractions. Using the algorithm proposed in [42] (Algorithm 2), we generate a Laguerre diagram in Ω with n grains such that grain i has volume r_i. This algorithm is initialized with generator points $x_1, \dots, x_N$. The final Laguerre diagram is approximately centroidal, meaning that the generator point of each cell is close to the center of mass of its cell (see Fig. 3).

Having generated a Laguerre diagram we take a random height z, sampled from the uniform distribution on $[0,1]$, and intersect the diagram with a horizontal plane at height z. Throughout, the diagrams we consider have periodic boundary conditions. If parts of a cell appear in a section multiple times (due to periodic boundary conditions) the areas of the parts are added together, and this sum is considered as a single observed area.

3. Simulation results

3.1. Laguerre diagrams

In this section, we apply the estimation procedure to randomly generated Laguerre diagrams. We apply the procedure described in

Section 2.2 100 times. By this we mean that 100 times, a Laguerre diagram is generated, a planar section is taken, and estimates of the grain volume distribution are computed under various shape assumptions.

For the following simulations we generate Laguerre diagrams with $N = 50000$ grains. We choose for the volume distribution F_V a lognormal distribution with parameters $\sigma = 0.4$, $\mu = -\frac{\sigma^2}{2}$. Each of the 100 runs generated a random sample of observed section areas whose sample sizes are shown in the left panel of Fig. 4.

The distribution of the observed section areas for one simulation is shown in the right panel of Fig. 4. For each of the shapes we consider, the simulation results are given in Figs. 5–6. Each blue line is an estimate corresponding to one of the 100 generated samples of section areas.

Looking at the estimates of the volume distribution, the estimates corresponding to the sphere and the tetrahedron are quite poor (Figs. 5 (b) and 6 (f)). One may argue that a sphere is 'too round' to be a good representation of a typical grain shape and the tetrahedron has 'too sharp corners' to be representative of a real grain. All other shapes yield much better estimates, in particular the estimates corresponding to the octahedron and the cube (Figs. 6 (b) and 6 (d)) appear quite close to the true volume distribution. The estimates corresponding to the biased volume distribution paint a similar, but slightly different picture. Note in particular that the variance of the estimates is rather different for each of the shapes. This variance is the smallest for the simulation results corresponding to the sphere, and largest for the results corresponding to the tetrahedron (Figs. 5 (a) and 6 (e)).
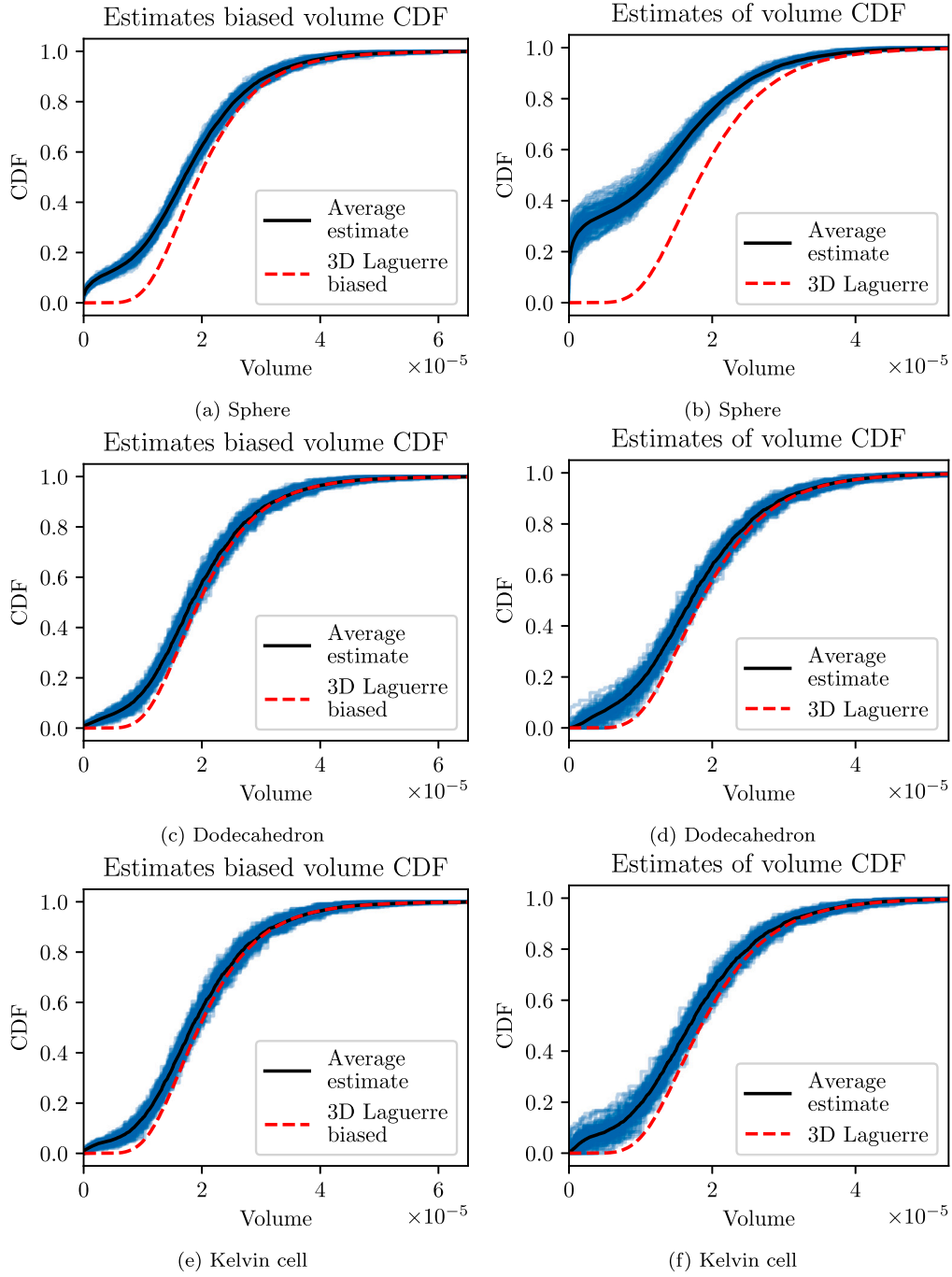
Fig. 5. Estimates of the biased volume distribution function (left) and estimates of the volume distribution function (right), based on the sphere, dodecahedron and Kelvin cell. The red dashed line represents F_V^b and F_V in the left and right panel respectively.

In Tables 1–2 errors of the estimates in Figs. 5 and 6 are shown. To be precise, the supremum error

$$\|\hat{F}_V - F_V\|_\infty := \sup_{x>0} \left| \hat{F}_V(x) - F_V(x) \right|.$$

and the L_1 error

$$\|\hat{F}_V - F_V\|_{L_1} := \int_0^\infty \left| \hat{F}_V(x) - F_V(x) \right| \mathrm{d}x.$$

are considered.

The results confirm what was found by the graphical inspection of Figs. 5 and 6. For the unbiased volume distribution function, both the supremum and the L_1 error suggest that the cube and the octahedron

are the best choice. What can be seen from both tables is that the sphere, the canonically used shape, leads to inferior approximations.

4. The choice of grain shape

In the previous section we have observed that some choices of grain shape yield much better results than other choices. We attempt to obtain a better understanding of why in particular the cube and the octahedron is often a good choice when the true data generating mechanism is Laguerre. To obtain preliminary results without making arbitrary choices on the distribution of weights, in this section Poisson–Voronoi diagrams that are Laguerre diagrams with all weights equal are used.
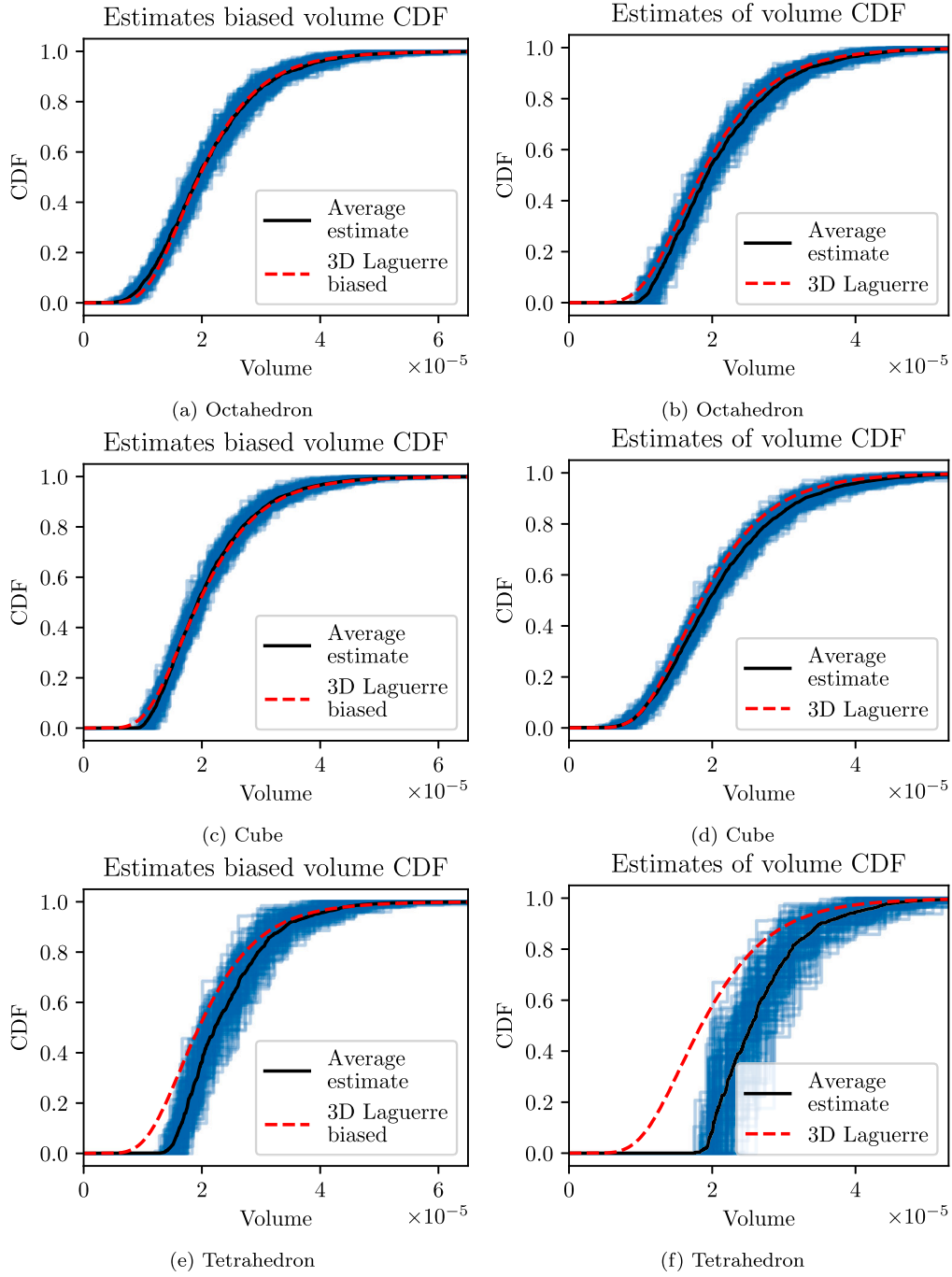
Fig. 6. Estimates of the biased volume distribution function (left) and estimates of the volume distribution function (right), based on the octahedron, cube and tetrahedron. The red dashed line represents F_V^b and F_V in the left and right panel respectively.

Table 1
Mean supremum errors of estimates for the unbiased and biased size distribution function with 2.5% and 97.5% quantiles based on 100 simulations.

	$\|\hat{F}_V - F_V\|_\infty$		$\|\hat{F}_V^b - F_V^b\|_\infty$	
Shape	Mean error	(2.5%, 97.5%)	Mean error	(2.5%, 97.5%)
sphere	0.391	(0.34 , 0.46)	0.196	(0.17 , 0.22)
dodecahedron	0.167	(0.13 , 0.21)	0.143	(0.12 , 0.17)
Kelvin cell	0.182	(0.14 , 0.23)	0.146	(0.12 , 0.17)
octahedron	0.154	(0.10 , 0.22)	0.118	(0.089, 0.16)
cube	0.134	(0.098, 0.17)	0.114	(0.081, 0.16)
tetrahedron	0.619	(0.52 , 0.75)	0.345	(0.28 , 0.41)

Table 2
Mean L_1 errors of estimates for the unbiased and biased size distribution function with 2.5% and 97.5% quantiles based on 100 simulations.

	$\|\hat{F}_V - F_V\|_{L_1}$ $(\times 10^{-6})$		$\|\hat{F}_V^b - F_V^b\|_{L_1}$ $(\times 10^{-6})$	
Shape	Mean error	(2.5%, 97.5%)	Mean error	(2.5%, 97.5%)
sphere	7.52	(6.37, 8.97)	3.51	(3.11 , 4.01)
dodecahedron	2.11	(1.42, 2.91)	1.91	(1.57 , 2.33)
Kelvin cell	2.41	(1.56, 3.74)	1.93	(1.61 , 2.34)
octahedron	1.46	(1.07, 1.97)	1.20	(1.00 , 1.45)
cube	1.45	(1.02, 1.99)	1.10	(0.850, 1.42)
tetrahedron	7.08	(5.29, 9.41)	3.54	(2.91 , 4.15)
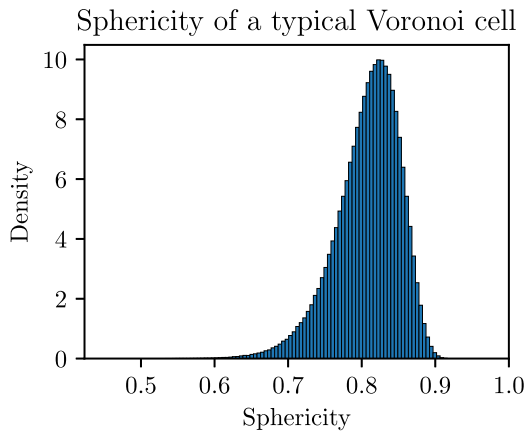
Fig. 7. Simulated distribution of sphericity of a typical Poisson–Voronoi cell, based on 10^6 Voronoi cells.

Fig. 8. Estimates of the volume distribution function of the cells of a Poisson–Voronoi diagram based on different shapes.

Table 3
Approximate sphericity of various convex shapes.

Shape	Sphericity
Sphere	1
Dodecahedron	0.910
Kelvin cell	0.910
Octahedron	0.846
Mean typical Voronoi cell	0.808
Cube	0.806
Tetrahedron	0.671

4.1. Characterizing shape via sphericity

Given a shape with volume V and surface area S, the isoperimetric inequality states:

$$S \geq \pi^{\frac{1}{3}} (6V)^{\frac{2}{3}},$$

Equality holds if and only if the shape is a sphere. It may also be stated as: among all shapes with a given surface area, a sphere has the maximum volume. In [43] this was used to define sphericity as:

$$\Psi = \frac{\pi^{\frac{1}{3}} (6V)^{\frac{2}{3}}}{S}.$$

Then, $\Psi = 1$ for a sphere and for any other shape $0 < \Psi < 1$. In [43] the sphericity of quartz particles was studied. It is challenging to determine when two grains have approximately the same shape. One approach is to consider grains with approximately equal sphericity as being close in shape. The use of sphericity is in any case arbitrary. Other shape parameters such ad the number of facets of vertices are other reasonable choice. Because we apply the estimation procedure to space-filling microstructures, one may wonder what is the average sphericity of a grain in such a microstructure. As previously mentioned, as an example we consider a Poisson–Voronoi diagram, where all weights equal. In [35,44] the sphericity has been used with other cell characteristics to describe the Poisson–Voronoi and the more general Laguerre diagram, respectively. Via simulations, we can generate Poisson–Voronoi cells and computing the sphericities of the individual cells yields the distribution in Fig. 7.

In Table 3 the sphericity of various convex shapes is given, as well as the estimated mean sphericity of a typical Voronoi cell. Clearly, among all considered shapes the sphericity of the cube is closest to the mean sphericity of a typical Voronoi cell.
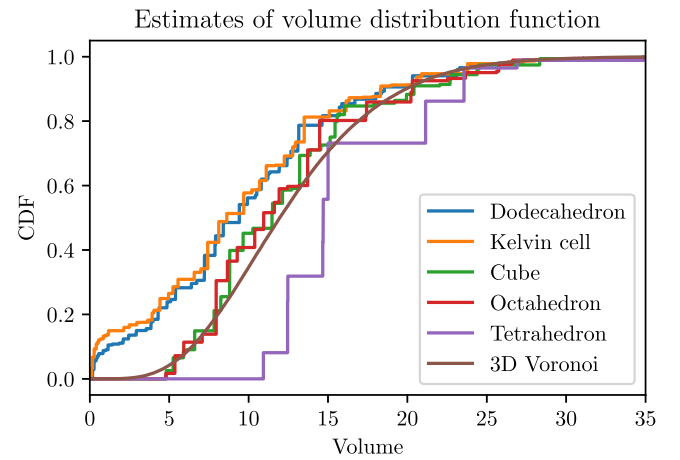
4.2. Verifying the choice of grain shape using the disector

A classical stereological technique for estimating the expected number of grains per unit volume N_V is called the disector [45]. It may also be used to estimate the mean grain volume since $\mathbb{E}(V) = 1/N_V$, for a space filling structure consisting of N_V cells in a unit volume body. The disector allows for unbiased estimation of N_V without assumptions on the grain shape. It requires two (close) parallel sections which are a known distance apart. Ideally, we would like to guarantee that no grains are lost between section planes, such that there are no grains between the two planes that we cannot observe. Let:

- Q^+: the number of grains which are observed in the top section but not in the lower section.
- Q^-: the number of grains which are observed in the lower section but not in the top section.
- A: the area of the observation window/ section plane.
- h: the distance between the section planes.

Then, N_V may be estimated via:

$$\hat{N}_V = \frac{Q^+ + Q^-}{2Ah}.$$

Let us first proceed as before, we have various shapes we can consider to estimate the grain volume distribution using a single section. The result of the simulation of one Poisson–Voronoi diagram are shown in Fig. 8. This particular realization of the Poisson–Voronoi diagram has 78862 cells.

For each of the estimates we can also compute the mean volume. We have estimates of the distribution function F_V denoted by $\hat{F}_V$. Then, the mean volume corresponding to $\hat{F}_V$ is given by:

$$\int_0^\infty x d\hat{F}_V(x).$$

In Table 4 the estimates for all the shape previously considered are shown.

In Fig. 9 mean grain volume estimates of the Poisson–Voronoi diagram are shown. These estimates are obtained using the disector method using 100 pairs of parallel section planes. The actual mean volume (red line in Fig. 9) is 12.68, which among the considered shapes, is closest to mean grain volume estimates obtained using the cube and the octahedron. In the context of this paper, we propose the disector method not as a tool for selecting an appropriate grain shape, but rather as a diagnostic approach to validate the grain shape assumptions made during the estimation process. In practice, one can take parallel sectional planes from a steel sample and then apply the
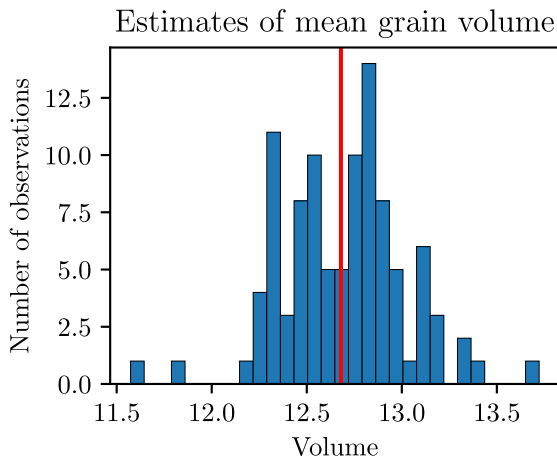
Estimates of mean grain volume

Fig. 9. Histogram of mean grain volume estimates of a Poisson–Voronoi diagram obtained using the disector. The red line indicates the actual mean volume.

Table 4
Estimated mean volume of the cells of a Poisson–Voronoi diagram corresponding to the estimates shown in Fig. 8 based on different shapes.

Shape	Estimated mean volume
Dodecahedron	9.959
Kelvin cell	9.621
Cube	12.35
Octahedron	12.35
Tetrahedron	16.20

disector technique to estimate the mean grain volume without any shape assumption. By comparing the estimated mean volumes from both a shape assumption and the disector method, which should ideally be close, one can validate whether a specific shape is a reasonable assumption for the given sample.

5. Application to experimentally measured EBSD data

In this section, we investigate an experimentally measured microstructure obtained using the Electron Backscatter Diffraction (EBSD) technique. The initial microstructure and crystallographic texture of the material were measured across the thickness (ND — normal direction) perpendicular to the rolling direction (RD) (see Fig. 10). The EBSD scan area is 500 µm × 500 µm. Standard metallographic techniques were used to prepare the specimen for characterization. Analysis of the EBSD data was performed using TSL OIM software. The material used in this study is Interstitial-Free (IF) steel. For this example, we have the 3D EBSD information available using the serial sectioning technique [22].

Following a standard postprocessing procedure, and discarding the small grains located at grain boundaries, we obtained a sample of 1506 fully observed grains A histogram of the observed section areas and a histogram of the observed grain diameters ($(\frac{4\,Area}{\pi})^{1/2}$) is shown in Fig. 11.

For all the shapes considered, we estimate the volume distribution function. These estimates can be directly compared to the experimental volume distribution in the 3D EBSD data set (Fig. 12)

From the comparison of the different shapes shown in Fig. 12 as in the Laguerre Voronoi simulation the cube and octahedron appear to be the best shapes.

6. Discussion

This paper critically addresses the problem of estimating 3D grain size distributions from 2D cross-sections, highlighting the importance
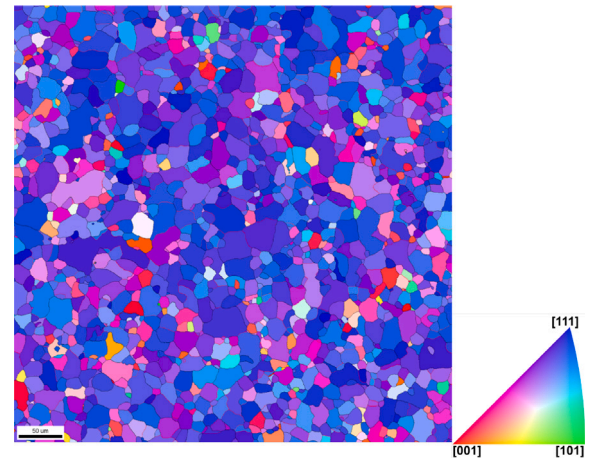

Fig. 10. Electron backscatter diffraction (EBSD) measurements of an IF steel sample. The figure shows the IPF color map parallel to the normal direction for a section of 500 µm × 500 µm.

of selecting an appropriate grain shape when applying the estimation procedure to space-filling microstructures. Our findings, supported by simulations using Laguerre Voronoi diagrams and a real-world data set, demonstrate that the choice of grain shape significantly affects the accuracy of the stereological estimates. Notably, our results suggest that while traditional shapes like spheres and tetrahedrons often provide poor estimates probably due to their geometric simplicity or complexity, shapes such as cubes and octahedrons yield more reliable results.

The use of the disector method, not as a selection tool for grain shapes but as a diagnostic tool, has utility potential. It provides a baseline for validating the assumptions made during the estimation process, ensuring that the chosen grain shape assumptions are reasonable for the given sample.

While the study has provided valuable insights into estimating 3D grain size distributions from 2D sections, there are natural challenges to be addressed in the future. One is related to the fact that our estimation method is inspired by a model considering 'randomly sized and -oriented shapes randomly positioned in the 3D medium' and applied to space-filling structures. It is interesting to develop methods really based on models (like Voronoi, Laguerre Voronoi or newly developed models such as generalized balanced power diagrams [46]) leading to space-filling structures.

The assumption of isotropy in the grain structures is another issue. The models considered assume that the morphological properties of the grains are uniform in all directions, which is often not the case in real-world materials. Many materials exhibit anisotropic behavior due to directional cooling, applied stresses, or processing methods that align the grains in particular orientations. Ignoring anisotropy can lead to significant deviations between the estimated and actual grain size distributions.

As it comes to the simulated data, the use of periodic boundary conditions is a practical approach to manage computational boundaries. However, this assumption may not accurately reflect the true edge conditions of real materials. In natural or manufactured materials, the boundary effects can significantly influence the microstructural features near the edges, which are not captured by periodic boundary conditions. This can skew the estimation of grain size distributions, especially for materials where edge effects are pronounced.

Sphericity, as well as other shape parameters, may help in shedding some light on why some shapes work better than others. However, in the current status, the estimation procedure proposed in this paper does not incorporate grain shape information as an input, instead it is specific for the assumed grain shape. As a future development, the
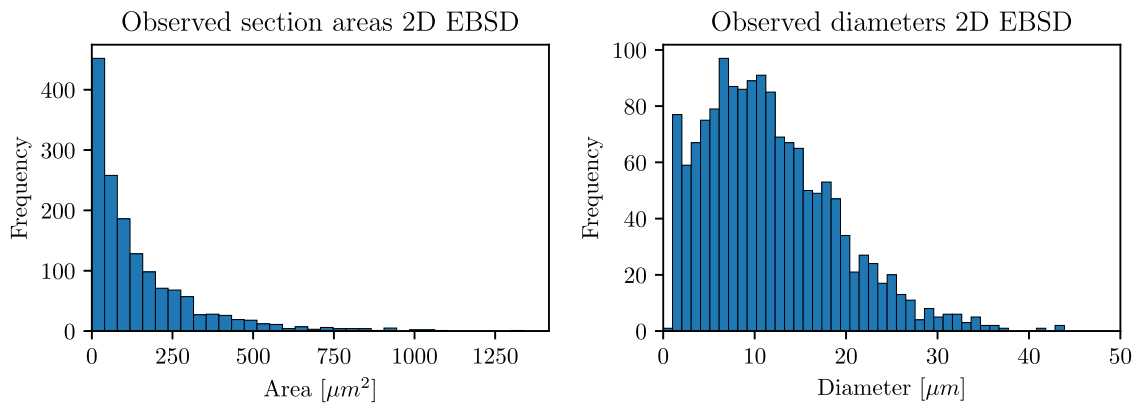
Fig. 11. Left: Observed grain areas in 2D EBSD data set. Right: Observed grain diameters in 2D EBSD data set.
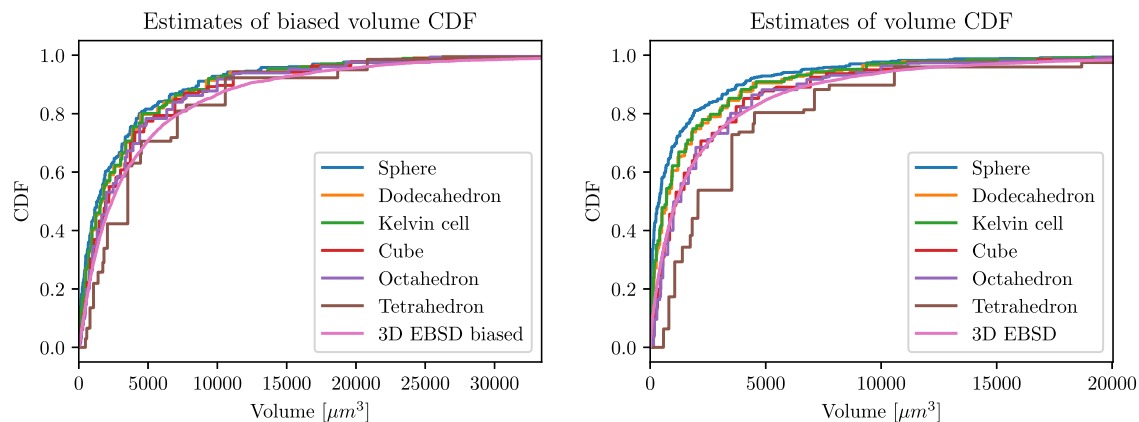

Fig. 12. Estimates of the biased volume distribution function (left) and estimates of the volume distribution function (right) based on different shapes.

inclusion of shape parameters as an input of an estimation procedure must be explored.

Finally, both the sphericity and the disector method look promising but they need to be validated using real data. Having sectional data and data on the 3D grain surface areas, one can use the disector method and the sphericity measure as diagnostic tools to validate the grain shape assumption made during the estimation process.

7. Conclusion

The results of this paper highlight the necessity for sensible grain shape selection in the estimation of 3D grain size distributions from 2D data. By using shapes that more accurately represent the microstructural characteristics of the material, such as cubes and octahedrons, we achieved more accurate stereological estimates. Future work should focus on enhancing these methodologies by integrating models that incorporate space-filling characteristics, anisotropy and more realistic boundary conditions. Developing these advanced models will enable more accurate and generally applicable tools in materials science, contributing to the understanding and characterization of complex materials.

CRediT authorship contribution statement

Thomas van der Jagt: Writing – review & editing, Writing – original draft, Visualization, Validation, Software, Methodology, Formal analysis, Conceptualization. **Martina Vittorietti:** Writing – review & editing, Writing – original draft, Supervision. **Karo Sedighiani:** Writing – review & editing, Writing – original draft, Supervision. **Cornelis Bos:** Writing – review & editing, Supervision. **Geurt Jongbloed:** Writing – review & editing, Supervision, Project administration.

Declaration of competing interest

The authors declare that they have no known competing financial interests or personal relationships that could have appeared to influence the work reported in this paper.

Data availability

Python scripts were used for simulating (Laguerre)-Voronoi diagrams, taking cross sections, estimating grain size distributions, and for performing all other analyses presented in this paper. These scripts are available in the public repository

https://github.com/thomasvdj/GrainSizeEstimation.

References

[1] D. Raabe, B. Sun, A. Kwiatkowski Da Silva, B. Gault, H.-W. Yen, K. Sedighiani, P. Thoudden Sukumar, I.R. Souza Filho, S. Katnagallu, E. Jägle, P. Kürnsteiner, N. Kusampudi, L. Stephenson, M. Herbig, C.H. Liebscher, H. Springer, S. Zaefferer, V. Shah, S.-L. Wong, C. Baron, M. Diehl, F. Roters, D. Ponge, Current Challenges and Opportunities in Microstructure-Related Properties of Advanced High-Strength Steels, Met. Mater. Trans. A 51 (11) (2020) 5517–5586.

[2] F. Roters, M. Diehl, P. Shanthraj, P. Eisenlohr, C. Reuber, S. Wong, T. Maiti, A. Ebrahimi, T. Hochrainer, H.-O. Fabritius, S. Nikolov, M. Friák, N. Fujita, N. Grilli, K. Janssens, N. Jia, P. Kok, D. Ma, F. Meier, E. Werner, M. Stricker, D. Weygand, D. Raabe, DAMASK – The Düsseldorf Advanced Material Simulation Kit for modeling multi-physics crystal plasticity, thermal, and damage phenomena from the single crystal up to the component scale, Comput. Mater. Sci. 158 (2019) 420–478.

[3] J.R. Mianroodi, N. H. Siboni, D. Raabe, Teaching solid mechanics to artificial intelligence—a fast solver for heterogeneous materials, Npj Comput. Mater. 7 (1) (2021) 99.

[4] M.S. Khorrami, J.R. Mianroodi, N.H. Siboni, P. Goyal, B. Svendsen, P. Benner, D. Raabe, An artificial neural network for surrogate modeling of stress fields in viscoplastic polycrystalline materials, Npj Comput. Mater. 9 (1) (2023) 37.

[5] M. Dao, M. Li, A micromechanics study on strain-localization-induced fracture initiation in bending using crystal plasticity models, Phil. Mag. A 81 (8) (2001) 1997–2020.

[6] F. Roters, P. Eisenlohr, L. Hantcherli, D. Tjahjanto, T. Bieler, D. Raabe, Overview of constitutive laws, kinematics, homogenization and multiscale methods in crystal plasticity finite-element modeling: Theory, experiments, applications, Acta Mater. 58 (4) (2010) 1152–1211.

[7] C. Tasan, J. Hoefnagels, M. Diehl, D. Yan, F. Roters, D. Raabe, Strain localization and damage in dual phase steels investigated by coupled in-situ deformation experiments and crystal plasticity simulations, Int. J. Plast. 63 (2014) 198–210, Deformation Tensors in Material Modeling in Honor of Prof. Otto T. Bruhns.

[8] M. Kasemer, P. Dawson, A finite element methodology to incorporate kinematic activation of discrete deformation twins in a crystal plasticity framework, Comput. Methods Appl. Mech. Engrg. 358 (2020) 112653.

[9] K. Sedighiani, K. Traka, F. Roters, J. Sietsma, D. Raabe, M. Diehl, Crystal plasticity simulation of in-grain microstructural evolution during large deformation of IF-steel, Acta Mater. 237 (2022) 118167.

[10] K. Sedighiani, V. Shah, K. Traka, M. Diehl, F. Roters, J. Sietsma, D. Raabe, Large-deformation crystal plasticity simulation of microstructure and microtexture evolution through adaptive remeshing, Int. J. Plast. 146 (2021) 103078.

[11] D.-K. Kim, W. Woo, W.-W. Park, Y.-T. Im, A. Rollett, Mesoscopic coupled modeling of texture formation during recrystallization considering stored energy decomposition, Comput. Mater. Sci. 129 (2017) 55–65.

[12] K. Traka, K. Sedighiani, C. Bos, J. Galan Lopez, K. Angenendt, D. Raabe, J. Sietsma, Topological aspects responsible for recrystallization evolution in an IF-steel sheet – investigation with cellular-automaton simulations, Comput. Mater. Sci. 198 (2021) 110643.

[13] V. Shah, K. Sedighiani, J. Van Dokkum, C. Bos, F. Roters, M. Diehl, Coupling crystal plasticity and cellular automaton models to study meta-dynamic recrystallization during hot rolling at high strain rates, Mater. Sci. Eng.: A 849 (2022) 143471.

[14] R. Armstrong, The influence of polycrystal grain size on several mechanical properties of materials, Met. Mater. Trans. 1 (5) (1970) 1169–1176.

[15] F. Barlat, Crystallographic texture, anisotropic yield surfaces and forming limits of sheet metals, Mater. Sci. Eng. 91 (1987) 55–72.

[16] N. Hansen, Hall–Petch relation and boundary strengthening, Scr. Mater. 51 (8) (2004) 801–806, Viewpoint set no. 35. Metals and alloys with a structural scale from the micrometer to the atomic dimensions.

[17] K. Sedighiani, M. Diehl, K. Traka, F. Roters, J. Sietsma, D. Raabe, An efficient and robust approach to determine material parameters of crystal plasticity constitutive laws from macro-scale stress–strain curves, Int. J. Plast. 134 (2020) 102779.

[18] K. Sedighiani, K. Traka, F. Roters, D. Raabe, J. Sietsma, M. Diehl, Determination and analysis of the constitutive parameters of temperature-dependent dislocation-density-based crystal plasticity models, Mech. Mater. 164 (2022) 104117.

[19] K. Somlo, B. Frodal, C. Funch, K. Poulios, G. Winther, O. Hopperstad, T. Børvik, C. Niordson, Anisotropic yield surfaces of additively manufactured metals simulated with crystal plasticity, Eur. J. Mech. A Solids 94 (2022) 104506.

[20] L. Wang, E. Mostaed, X. Cao, G. Huang, A. Fabrizi, F. Bonollo, C. Chi, M. Vedani, Effects of texture and grain size on mechanical properties of AZ80 magnesium alloys at lower temperatures, Mater. Des. 89 (2016) 1–8.

[21] N. Allain-Bonasso, F. Wagner, S. Berbenni, D.P. Field, A study of the heterogeneity of plastic deformation in IF steel by EBSD, Mater. Sci. Eng.: A 548 (2012) 56–63.

[22] H. Pirgazi, On the alignment of 3D EBSD data collected by serial sectioning technique, Mater. Charact. 152 (2019) 223–229.

[23] S. Wicksell, The corpuscle problem. A mathematical study of a biometric problem, Biometrika 17 (1925) 84–99.

[24] S.A. Saltikov, The determination of the size distribution of particles in an opaque material from a measurement of the size distribution of their sections, in: H. Elias (Ed.), Stereology, Springer Berlin Heidelberg, 1967, pp. 163–173.

[25] M.A. Lopez-Sanchez, S. Llana-Fúnez, An extension of the Saltykov method to quantify 3D grain size distributions in mylonites, J. Struct. Geol. 93 (2016).

[26] J.N. Cuzzi, D.M. Olson, Recovering 3D particle size distributions from 2D sections, Meteorit. Planet. Sci. 52 (2017) 532–545.

[27] S. Benito, C. Cuervo, F. Pöhl, W. Theisen, Improvements on the recovery of 3D particle size distributions from 2D sections, Mater. Charact. 156 (2019) 109872.

[28] J. Ohser, M. Nippe, Stereology of cubic particles: various estimators for the size distribution, J. Microsc. 187 (1997) 22–30.

[29] R. McAfee, I. Nettleship, The simulation and selection of shapes for the unfolding of grain size distributions, Acta Mater. 51 (2003) 4603–4610.

[30] K. Mehnert, J. Ohser, P. Klimanek, Testing stereological methods for the estimation of spatial size distributions by means of computer-simulated grain structures, Mater. Sci. Eng.: A 246 (1998) 207–212.

[31] F. Yin, A. Sakurai, X. Song, Determination of spatial grain size with the area-weighted grain area distribution of the planar sections in polycrystalline materials, Met. Mater. Trans. A 37 (2006) 3707–3714.

[32] S.N. Chiu, D. Stoyan, W.S. Kendall, J. Mecke, Stochastic Geometry and its Applications, John Wiley & Sons, Ltd, 2013.

[33] T. van der Jagt, G. Jongbloed, M. Vittorietti, Stereological determination of particle size distributions for similar convex bodies, Electron. J. Stat. 18 (2024) 742–774.

[34] A. Okabe, B. Boots, K. Sugihara, S.N. Chiu, Spatial Tessellations: Concepts and Applications of Voronoi Diagrams, John Wiley & Sons, 2009.

[35] J. Meijering, Interface area, edge length, and number of vertices in crystal aggregates with random nucleation, Philips Res. Rep. 8 (1953) 270–290.

[36] C. Lautensack, Fitting three-dimensional Laguerre tessellations to foam structures, J. Appl. Stat. 35 (2008) 985–995.

[37] A. Gusakova, Z. Kabluchko, C. Thäle, The β-Delaunay tessellation: Description of the model and geometry of typical cells, Adv. in Appl. Probab. 54 (4) (2022) 1252–1290.

[38] Z. Fan, Y. Wu, X. Zhao, Y. Lu, Simulation of polycrystalline structure with Voronoi diagram in Laguerre geometry based on random closed packing of spheres, Comput. Mater. Sci. 29 (2004) 301–308.

[39] A. Liebscher, Laguerre approximation of random foams, Phil. Mag. 95 (2015) 2777–2792.

[40] S. Falco, J. Jiang, F. De Cola, N. Petrinic, Generation of 3D polycrystalline microstructures with a conditioned Laguerre-Voronoi tessellation technique, Comput. Mater. Sci. 136 (2017) 20–28.

[41] Y. Wu, W. Zhou, B. Wang, F. Yang, Modeling and characterization of two-phase composites by Voronoi diagram in the Laguerre geometry based on random close packing of spheres, Comput. Mater. Sci. 47 (2010) 951–961.

[42] D.P. Bourne, P.J.J. Kok, S.M. Roper, W.D.T. Spanjer, Laguerre tessellations and polycrystalline microstructures: a fast algorithm for generating grains of given volumes, Phil. Mag. 100 (2020).

[43] H. Wadell, Volume, shape, and roundness of quartz particles, J. Geol. 43 (1935) 250–280.

[44] F. Seitl, J. Møller, V. Beneš, Fitting three-dimensional Laguerre tessellations by hierarchical marked point process models, Spat. Stat. 51 (2022) 100658.

[45] D. Sterio, The unbiased estimation of number and sizes of arbitrary particles using the disector, J. Microsc. 134 (2) (1984) 127–136.

[46] A. Alpers, A. Brieden, P. Gritzmann, A. Lyckegaard, H.F. Poulsen, Generalized balanced power diagrams for 3D representations of polycrystals, Phil. Mag. 95 (9) (2015) 1016–1028.